

## IMAGING SPECTROPHOTOMETRY OF THE PLANETARY NEBULA NGC 6720 (THE RING NEBULA)

NANCY JOANNE LAME AND RICHARD W. POGGE

Department of Astronomy, The Ohio State University, Columbus, Ohio 43210  
Electronic mail: lame@payne.mps.ohio-state.edu, pogge@keeler.mps.ohio-state.edu

*Received 1994 June 3*

### ABSTRACT

Detailed emission-line imaging of the planetary nebula NGC 6720 (the Ring Nebula) is presented. We map emission-line fluxes of the lines [N II] $\lambda\lambda$ 5755,6583, [S II] $\lambda\lambda$ 6717,6731, [O I] $\lambda$ 6300, [O III] $\lambda$ 5007, He II  $\lambda$ 4686, H $\alpha$ , and H $\beta$  using the Ohio State Imaging Fabry–Perot Spectrograph. From these fluxes we derive maps of the [N II] electron temperature, [S II] electron density, Balmer decrement, and ionization diagnostics across the nebula. A sharp drop in ionization is seen along the entire outer edge of the nebula and the ionization edge is resolved and clumpy. We show that the [O I]-bright filaments are not substantially denser or cooler than the gas in which they are embedded. The [S II] density map shows two strong, clumpy density enhancements on the minor axis of the nebula, inside the outer edge. These density enhancements motivate our model of an oval-shaped toroid for the nebula.

### 1. INTRODUCTION

Within a planetary nebula (PN), the density, temperature, and ionization state can vary significantly not just as a function of distance from the central star, but also in each direction from the central star. Emission-line spectroscopy can be used to study these physical parameters across the nebula. Most previous spectrophotometric studies of the Ring Nebula, the most notable of which are Dufour & Quigley (1993), Hawley & Miller (1977), and Barker (1987), have been limited to only partial spatial coverage, which only measures the physical conditions in a small portion of the nebula. Two-dimensional spectrophotometry using narrow-band filter imaging, which covers the whole nebula, has been done by Reay & Worswick (1977) and Kupferman (1983). This method of narrowband filter imaging is difficult, however, (see Jacoby *et al.* 1987) and can be problematic due to contamination of the filter bandpass from nearby lines. In the Ring Nebula this is a particularly troublesome problem due to strong [N II] $\lambda$ 6583 relative to H $\alpha$ , making contamination between bands significant. The [S II] $\lambda$ 6717/6730 density diagnostic depends on small differences in intensity between the two closely spaced lines, making conventional narrow-band filter imaging less accurate.

When closely spaced lines need to be observed, more accurate two-dimensional spectroscopy can be accomplished using Fabry–Perot interferometry. The utility of this technique has been demonstrated in a recent study of the Orion Nebula by Pogge *et al.* (1992). In this paper we present a study of the Ring Nebula that uses a combination of Fabry–Perot interferometry, narrowband filter imaging, and long-slit spectrophotometry to achieve good spatial and spectral resolution of emission lines. We make maps of emission-line ratios measuring the Balmer decrement, electron density in the S<sup>+</sup> zone, electron temperature in the N<sup>+</sup> zone, and ionization state.

Besides yielding a large increase in the number of points in the nebula in which we know the physical conditions,

two-dimensional maps also make it easier to discern patterns that might otherwise go unnoticed. For example, it is possible to look at the entire outer edge of the nebula, all the filamentary regions, and specific morphological components. The large spatial coverage of our data combined with its more accurate spectral resolution allows us to investigate the ionization edge, the filaments, and the geometry of the Ring Nebula.

As discussed by Balick *et al.* (1992), the Ring Nebula at first glance appears to fit the classical model of an ionization bounded nebula. Ionization is observed to be radially stratified, with high ionization lines such as He II produced closer to the central star than low ionization lines such as [N II] (Reay & Worswick 1977). Molecular hydrogen is observed along the outer edge of the nebula (coincident with the [O I] emission) (Greenhouse *et al.* 1988; Zuckerman & Gatley 1988; Kastner *et al.* 1994). The Ring Nebula, however, has two partially ionized halos that are outside, or at least are projected outside of the ionization front (Balick *et al.* 1992). Kinematical observations of the Ring Nebula show that the inner halo is probably bipolar and projected outside the ionization front (Bryce *et al.* 1994). There is no such evidence for the outer halo. The ionization front can be studied in detail with our data because the entire outer edge of the nebula is continuously covered. The intensity of low ionization potential lines, especially [O I], with respect to high ionization lines, indicates conditions at the edge of the nebula.

When the nebula is imaged in the [N II] and [O I] emission lines, it has a very filamentary appearance. Emission from the low ionization potential (LIP) species O<sup>0</sup> and N<sup>+</sup> is quite strong in the Ring Nebula compared to other PNs (Campbell 1968; Hawley & Miller 1977). Filamentary-looking nebulae are expected when [O I] line emission is strong (Kaler 1980) because strong [O I] emission requires the presence of cool, optically thick, dense condensations (Williams 1973). [O I] emission can be produced in the observed amounts by the ionized “skins” of the condensations and the “shadowed” regions behind them. These shadowed

regions, which appear as filaments, are shielded from the radiation from the central star and are photoionized by diffuse nebular radiation. While Boeshaar (1974) found the expected higher densities in the filaments of the Ring Nebula, other studies (Hawley & Miller 1977; Kupferman 1983) have claimed that no density enhancements existed in the filaments. With our two-dimensional spectrophotometry, we study the physical conditions across the filaments in order to compare to these models and to observations of filaments in other PN.

The geometry of the Ring Nebula has never been firmly established. Fabry–Perot kinematics of the high ionization [O III] $\lambda$ 5007 emission show a spherical expansion (Atherton *et al.* 1978), and Kupferman (1983) found that He II emission is consistent with a closed sphere geometry. These lines, however, arise primarily from the hot inner regions immediately surrounding the central star. It has long been known that emission from low ionization lines, such as [N II] and even the hydrogen Balmer lines, has a distribution that is *not* consistent with a spherical geometry and indicates a deficit of material of these ionization species along the line of sight to the central star of the Ring Nebula (Curtis 1918; Kupferman 1983). Minkowski & Osterbrock (1960) suggested that the Ring Nebula is a bipolar nebula similar to NGC 650–1 that is being viewed along the polar axis. Recently, Volk & Leahy (1993) also suggested this based on their deprojected emission images.

Current models of planetary nebula structure and evolution are based on the interacting stellar winds theory (Kwok *et al.* 1978). In the simplest case of these models, a fast (1000 km/s) tenuous wind from the central star interacts with a slow dense AGB mass-loss wind. The fast wind creates a hot bubble core which expands and snowplows material in the AGB wind into a thin shell. The morphologies of many PNs can be explained by a density gradient (from equator to pole, generally with a higher equatorial density) in the ABG wind (Balick 1987). Because the hot bubble expands faster in the lower density polar direction, three basic morphological types are created depending upon the density contrast: a uniform density produces spherical nebulae, a low density contrast produces elliptical nebulae, and a high density contrast produces butterfly-shaped nebulae. We use our electron density map and emission-line flux images to place constraints on the possible geometry of the Ring Nebula, *vis-à-vis* these basic forms.

In Sec. 2, we detail the observations and data analysis. In Sec. 3, we describe the results, namely, the line flux maps and diagnostic emission-line ratio maps. A discussion and summary follows in Sec. 4.

## 2. OBSERVATIONS AND DATA REDUCTION

In this section we describe the observations and data reductions. Using Fabry–Perot spectroscopy for measuring emission-line flux maps is an unconventional technique. We demonstrate that our results are comparable to long-slit spectroscopy in accuracy, but with extended spatial coverage.

TABLE 1. Data cubes.

Lines	$\lambda\lambda$	Exposure	$N_{\text{images}}$	# Spectra	Seeing	Date
H $\alpha$ , [N II]	6523–6596	180 s	33	6328	2.8"	May 1991
[S II]	6690–6758	300 s	36	4514	2.0"	June 1992

### 2.1 Observations

All observations of the Ring Nebula were obtained with the 1.8 m Perkins Telescope in Flagstaff AZ. The full data set is comprised of single emission-line images, data cubes covering more than one emission line, and calibration long-slit spectra. The advantage of observing a spectroscopic data cube of the lines of interest over conventional narrowband filter imaging techniques is twofold. First, because closely spaced lines such as H $\alpha$ , [N II] $\lambda$ 6548,6583, and [S II] $\lambda\lambda$ 6717,6731 are deblended using model (Lorentzian) line profiles, we can obtain uncontaminated line fluxes. Second, the line fitting procedure also calculates continuum fluxes at the line wavelengths, providing a more accurate estimate of the continuum than would be obtained by extrapolating off-band images. We emphasize that we are not simply using the Fabry–Perot as a crude tunable filter, but as a true three-dimensional spectrograph with the expressed goal of calibrated imaging spectrophotometry.

The Imaging Fabry–Perot Spectrograph (IFPS) (more fully described in Pogge *et al.* 1992) was used for acquisition of the data cubes. The IFPS is a focal reducing camera using a Queensgate ET50 Fabry–Perot etalon with a TI 800 $\times$ 800 CCD detector at a pixel scale of 0.5"/pixel. A low-resolution etalon (200 km/s) was used, producing a spectral resolution in the data cubes of about 4 Å FWHM. This resolution is insufficient to resolve the expansion velocity of the nebula (26 km/s, Weinberger 1989), but well suited for clearly resolving the H $\alpha$ + [N II] and [S II] line blends. All line profiles are determined by the instrumental profile, which is well approximated by a Lorentzian function. Our observations were taken in the form of two data cubes, centered at  $\lambda$ 6563 (H $\alpha$  and [N II] lines) and  $\lambda$ 6724 ([S II] $\lambda\lambda$ 6717,6731 doublet) in May 1991 and June 1992. In Table 1 we list the wavelength coverage (Col. 2), exposure time of each frame (Col. 3), number of interferograms in each data cube (Col. 4), the number of spectra that were fit in each data cube (Col. 5), and the seeing during the data cube observations (Col. 6). Since the IFPS has no temperature control, the etalon was monitored for reactions to changes in ambient dome temperature and continually adjusted during observations for the [S II] data cube. We saw no evidence of wavelength variation due to etalon temperature changes in the H $\alpha$  data cube line profiles.

Since using the IFPS in spectroscopic mode (with the etalon) requires several hours of photometric conditions, it is more efficient to observe isolated lines in direct imaging mode using narrowband filter techniques (Pogge 1992). In direct imaging mode, the etalon is removed from the IFPS, making it a conventional focal-reducing system. We observed the He II  $\lambda$ 4686, H $\beta$ , [O III] $\lambda$ 5007, [N II] $\lambda$ 5755, and [O I] $\lambda$ 6300 emission lines in this mode during June and September 1992 (see Table 2). Continuum images were made by

TABLE 2. Direct images.

Line	Filter		Exposure	Seeing(")	Date
	Bandpass	Tilt(°)			
He II	4692/56	0	2400 s	1.5	Sept 1992
H $\beta$	4861/30	0	1200 s	2,1.5	June, Sept 1992
cont. (H $\beta$ )	4861/30	15	1200 s	1.5	Sept 1992
[O III]	5007/30	0	540 s	2	June 1992
[N II]	5755/30	0	1200 s	2	June 1992
cont. ([N II])	5755/30	15	1200 s	2	June 1992
[O I]	6300/30	0	900 s	2	June 1992
cont. ([O I])	6300/30	15	900 s	2	June 1992
[O I]	6300/30	0	2700 s	1.5	Sept 1993
cont. ([O I])	6300/30	15	2700 s	1.5	Sept 1993

“tilt tuning” several of the filters 15° to observe the blue side continuum. Field star profiles in the continuum images were not distorted, evidence that tilting filters does not introduce undesirable effects in the images.

Relative flux calibration between the data cubes and individual direct images was accomplished using flux-calibrated long-slit spectra of known positions in the nebula. The long-slit spectra were obtained on the 1.8 m Perkins Telescope in June 1992 and June 1993 using the Boller & Chivens CCD spectrograph with a 350 ln/mm grating (FWHM=5 Å). The slit was placed on the central star, and oriented along position angle 90° (1992) and 129° (1993). The slit width was 2" and had a length of 3.5 (unvignetted portion). It was not possible to obtain the entire spectral range on one spectrum, so two spectra covering the range were taken. The wavelength ranges were  $\lambda 4725\text{--}5952$  Å and  $\lambda 5613\text{--}6848$  Å for the 1992 long-slit spectra and  $\lambda 4250\text{--}5475$  Å and  $\lambda 5630\text{--}6870$  Å for the 1993 long-slit spectra. The 1992 spectra were used for all flux calibrations except the He II  $\lambda 4686$  image.

### 2.2 Data Cube Analysis

The data cubes were analyzed using the data cube reduction package OASIS (Pogge 1991). The spectral line parameters (line center, total flux, and FWHM), continuum, and rms uncertainty of the line profile fit were measured at each location in the object and assembled into maps of flux, continuum, etc., across the nebula. Fits can be made to  $\pm 2\%$  rms of residuals of the data and fit, and fits worse than  $\pm 10\%$  were not accepted. In low S/N spectra, the most difficult problem was in fitting the continuum, which contributed the major portion of the uncertainty to the fit. A mask over the field of view was applied before analysis of the data cubes to remove spectra with very faint emission. The edge of the mask is slightly outside the sharp edge of emission, and none of the structures observed are artifacts caused by masking.

Although both data cubes were analyzed in a similar manner, analysis of each data cube had its own idiosyncrasies. For the H $\alpha$  data cube, the FWHMs for all three lines were constrained to be a specific number (i.e., the instrumental width). This was necessary because the spectra are slightly undersampled in wavelength. The regions selected for continuum determination were weighted to the blue side of the spectra to avoid contamination of the continuum with [N II] emission, due to the inherently large Lorentzian wings in the

line. The H $\alpha$  continuum measured in the data cube does not show a more filamentary structure than the direct image continuum at  $\lambda 6300$ , and so we do not see significant contamination from [N II]. For the [S II] cube, the FWHM was allowed to vary as a function of position, however we constrained the FWHM of the two lines to be the same. Because the [S II] emission in the center of the nebula is weak relative to the continuum, we were not able to make good fits to the lines in that region.

To investigate the halo, where emission is too faint for line fitting in the data cubes, integration over wavelength bands was used in the data cube. Integration is over simulated “on-band” and “off-band” top-hat filters, and contamination from the wings of neighboring emission lines can be corrected for by assuming the measured instrumental profile. Although results from band averaging are slightly less accurate than those from line fitting in bright regions, we used this technique only for inherently low flux spectra where the nonlinear least-squares fitting procedure gave fits with large variations in parameters or unacceptably large rms residuals.

### 2.3 Emission-Line Image Analysis

The images taken with the IFPS in direct-imaging mode were reduced with IRAF using standard techniques. The optics on the IFPS were upgraded between June and September, and so the two sets of images are kept separate to avoid introducing an additional source of error from the necessary geometric coordinate transformation. The [N II] $\lambda 5755$  and [O I] $\lambda 6300$  images used in the final analysis were corrected for nebular continuum emission with off-band images using the same filter. In these weak lines, the nebular continuum was a significant contribution to the on-band image (22% of [N II] $\lambda 5755$ ). The He II image was corrected for nebular continuum observed with the tilted (off-band) H $\beta$  filter. A continuum image near H $\beta$  was not obtained in June 1992. However, the nebular continuum emission is weak at  $\lambda 4861$ , about 2% of H $\beta$  flux. This was determined by comparing the total flux in the Sept. 1992 H $\beta$  image to the total flux in the Sept. 1992 continuum subtracted H $\beta$  image, as well as from the long-slit observations. Because the continuum contribution in H $\beta$  is small, subtraction of nebular continuum from the June 1992 H $\beta$  image was not necessary as it did not affect line-ratio maps.

There was some contamination by adjacent lines in our narrowband filter images, but in all cases it was small enough that our results were not significantly affected. The [O I] $\lambda 6300$  image is contaminated by [S III] $\lambda 6312$  emission that falls inside the wing of the filter bandpass (filter transmission  $T_{\lambda 6312} = 0.4 T_{\lambda 6300}$ ). Long-slit spectroscopy shows that the [S III] emission is weak ([S III] $\lambda 6312$ /[O I] $\lambda 6300 = 0.01\text{--}0.05$  in strong [O I] emission regions, depending on radius), and limited in extent to the inner, high-ionization core of the nebula where it is strongly correlated with [O III] $\lambda 5007$  emission. Thus, in the outer [O I]-bright regions, we expect little contamination of the [O I]. The He II image is also slightly contaminated by the weak adjacent lines [Ar V] and He I  $\lambda 4711$  that fall inside the filter bandpass. Longslit spectra show this blended line has a maximum

strength of  $\sim 7.5\%$  of He II  $\lambda 4686$  strength. In the H $\beta$  bandpass, no correction was made for the He II  $\lambda 4859$  line as the contribution should be less than 1.5% (Brocklehurst 1971; Richer *et al.* 1991). Overall, contamination in any direct image was not large enough to cause problems.

Although the direct images and the [S II] data cube all have comparable seeing, the H $\alpha$  data cube was taken during 3" seeing and so it is necessary to match the point spread functions between images whenever constructing ratio maps with H $\alpha$  or [N II] $\lambda 6583$  (the two diagnostic maps affected are the [N II] temperature map and the Balmer decrement map). This is particularly important in the Ring Nebula due to the spatially sharp changes in intensity formed by the filaments and the outer edge of the nebula. The direct image was first registered with respect to the H $\alpha$  data cube, then smoothed to 3" effective seeing using a Gaussian kernel. The smoothing kernel width was determined by comparing the stellar point spread functions in H $\alpha$  data cube mash (the sum of all the interferograms in the cube) and the direct image (not continuum subtracted).

#### 2.4 Flux Calibration

To calibrate our data cubes and direct image fluxes we compared them to flux-calibrated long-slit spectra. Long-slit spectra at PA=90° were used. The regions used for sky subtraction in the long-slit spectra were at a radius of about 100", which is still within the faint halo of the nebula [Balick *et al.* (1992) give an outer halo diameter of 270"]. Faint nebular emission lines from the halo could be seen in the sky spectrum (the strongest, [N II] $\lambda 6583$ , had a peak about 3.5 times sky level). These emission lines were removed from the sky spectrum by interpolation from spectrally adjacent regions. The only nebular emission line for which this was not done was the [O I] $\lambda 6300$  line, which is blended with the strong [O I] night sky line. Our [O I] image shows [O I] emission is very weak in the outer halo except at the extreme edges. We estimate that nebular [O I] contribution is no more than 12% of the [O I] night sky line. Thus, sky may be slightly oversubtracted in the long-slit spectra on that particular line. Apertures (3"×2") along the slit were extracted, and all emission lines were fit using a Gaussian profile where possible. (The flux for weak emission lines was measured using band integration.)

Calibration of the emission-line images (both Fabry-Perot and filter) was done individually for each line, and as can be seen in Fig. 1, we have achieved photometric accuracy comparable to our long-slit spectrographic observations. Fabry-Perot derived line ratios for [N II] $\lambda 6583$ /H $\alpha$  are in excellent agreement with the long-slit ratio. The flux calibrations show the need for minor corrections to account for structure in the order-separation filter transmission curve. This white-light correction is seen as a 25% difference between the H $\alpha$  and [N II] $\lambda 6583$  flux calibrations. Long-slit calibrations for the  $\lambda\lambda 6717, 6731$  lines showed that data cube also required a small white light correction (3%). We stress that the relative flux calibration is very accurate, to 5%, but the absolute flux calibration is not as well determined (30%)

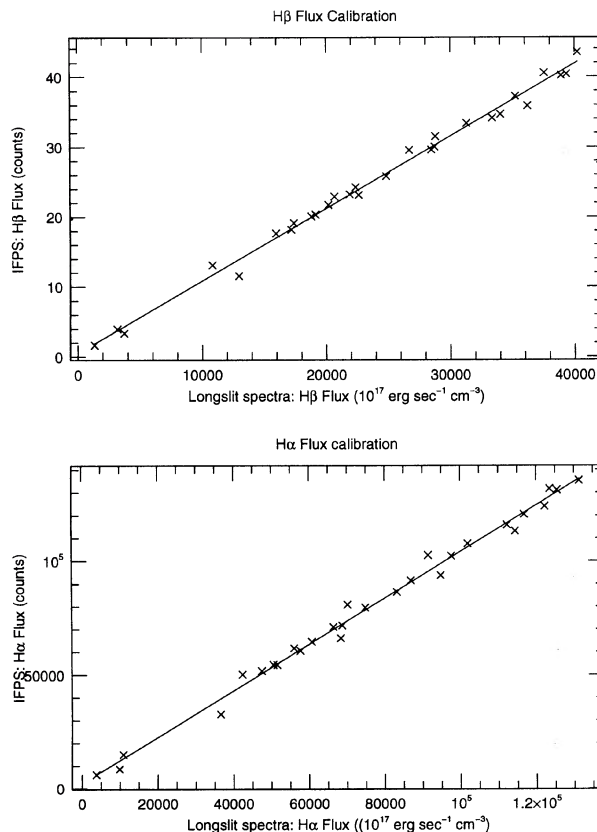


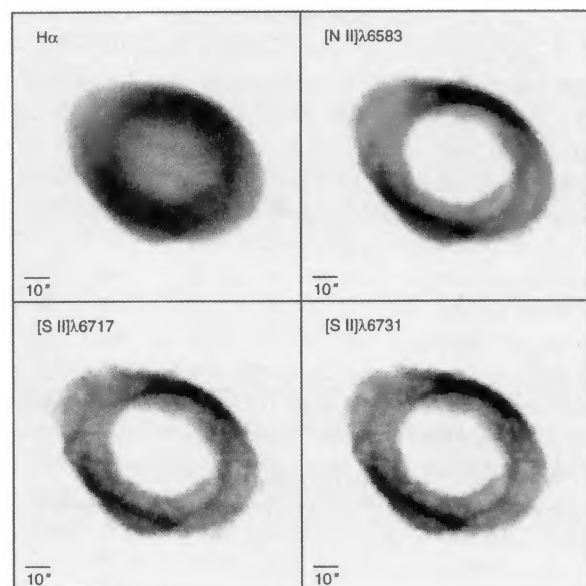
FIG. 1. Flux calibration. Squares plotted are H $\alpha$  (a) or H $\beta$  (b) flux in 2"×2" apertures situated along a cut PA=90° through the central star. Intensity from the image (x axis) is plotted vs flux from the long-slit spectra ( $10^{-17}$  erg s $^{-1}$  cm $^{-3}$ ). The solid line represents a least-squares fit to the points; the slope of the line is the flux calibration.

since the calibration long-slit spectra were not taken in photometric conditions.

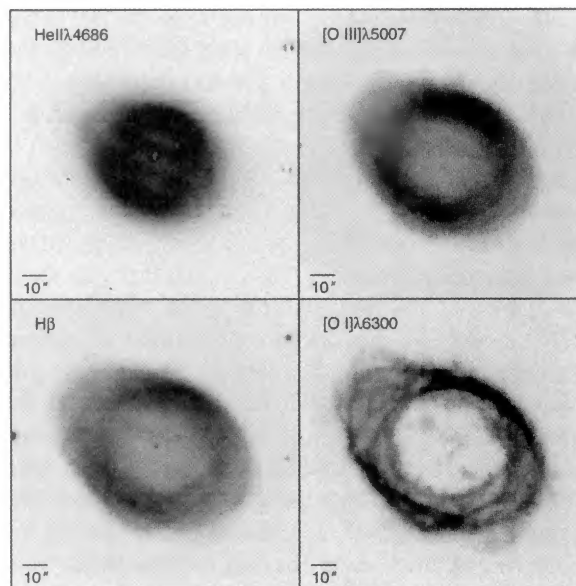
Images used in ratio maps have been corrected for extinction using the interstellar extinction curve of Cardelli *et al.* (1989) and using  $A_V=0.69$  ( $c=0.322$ ) derived from the ratio of the integrated H $\alpha$  and H $\beta$  fluxes (discussed in Sec. 3.3), assuming an intrinsic Case B recombination ratio of 2.86. Because the reddening is small, using a different intrinsic ratio will not affect the data significantly. The variation in observed Balmer decrement across the nebula is also small, and so a constant correction is acceptable.

### 3. RESULTS

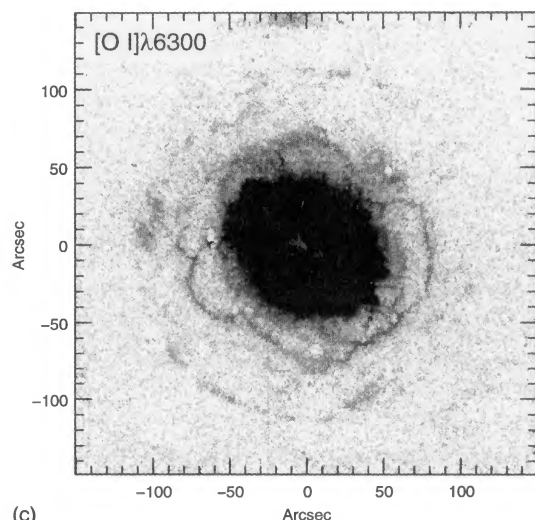
We present the final line-emission and line-ratio maps in this section. A definition of our morphological terminology is followed by a description of the line flux maps in Sec. 3.1. In Sec. 3.2 we present maps of physical conditions in the nebula (electron density, etc.) with a description of how we estimate these physical quantities and an estimation of errors. We compare these results to previous spectrophotometric studies, particularly Barker (1987), Hawley & Miller (1977), and Kupferman (1983). We also present results from our calibration long-slit spectra when relevant.



(a)



(b)



(c)

### 3.1 Line Flux Maps

We identify two important morphological features: the shell and the core. The shell is the bright “ring” of the nebula with a round inner radius of  $20''$  and an outer elliptical semimajor axis of  $50''$ . The core is the inner  $20''$  of the ring, and appears as the “hole” in the center of the shell. We shall adopt this terminology throughout the rest of the paper. Note that Balick *et al.* (1992) refer to the ring as the core of the nebula. However, their morphological assessment does not allow us to distinguish between the ring and the hole. In general, the Ring Nebula does not fit Balick’s (1993) bright rim+attached shell morphological picture of a PN, hence the confusion. Emission-line flux images from data cube reductions and direct images are shown in Fig. 2. Below we discuss the emission features in each of the three morphological components: the shell, the core, and the halo.

Flux from most emission lines is strongest in the shell. As has been noted before by Capriotti *et al.* (1971), the images show varying amounts of filamentary structure depending upon the emission line imaged. In general, higher ionization

FIG. 2. (a) Line flux maps from the data cubes.  $H\alpha$ ,  $[N\ II]\lambda 6583$ ,  $[S\ II]\lambda 6717$ ,  $[S\ II]\lambda 6731$ . Images are  $120''$  across, with north at the top and east to the left. Flux is zero where the data cube was masked and no spectra were fit. (b) Line flux maps from direct imaging.  $He\ II\ \lambda 4686$ ,  $[O\ III]\lambda 5007$ ,  $H\beta$ ,  $[O\ I]\lambda 6300$ . Images are  $120''$  across, oriented with north at the top and east to the left. The  $He\ II$  and  $[O\ I]$  images have been corrected for nebular continuum. (c)  $[O\ I]\lambda 6300$  emission. This image was obtained Sept. 1993. Contrast has been adjusted to clearly show the inner and outer halo and edge brightening.

images are smoother [e.g.,  $[O\ III]\lambda 5007$ , Fig. 2(b)] and lower ionization images are more filamentary, with the  $[O\ I]$  image [Fig. 2(b)] showing extreme filamentary structure. In the  $[O\ I]$  images, radial scalloped-like features can be seen in the filaments along the inner edge of the shell.

The central core is strong primarily in high ionization potential (HIP) lines.  $He\ II\ \lambda 4686$  emission (Fig. 2) fills the center inside the bright shell. The  $He\ II$  emission is rounder than the emission (e.g.,  $H\alpha$ ) in the surrounding shell. Reay & Worswick (1977) showed that there is relationship between ionization potential and apparent ellipticity of the nebula in a particular emission line, with the nebula appearing rounder in images of higher ionization potential lines. Structure can be seen in the  $He\ II$  images in the form of bands across the nebula parallel to the major axis. These stand out quite clearly in the  $He\ II\ \lambda 4686$  images (about 15% brighter than surrounding emission) and can also be seen traversing the center of the nebula in the  $H\alpha$ ,  $H\beta$ , and  $[O\ III]$  emission-line images (Fig. 2). Although low ionization emission lines such as  $[O\ I]$  are extremely weak in the core, anomalous structures

can be seen in these lines (the most obvious is the two blobs of emission inside the hole seen in the [O I] image).

In general, our observations of the halo confirm the findings of Chu *et al.* (1987); Moreno & López (1987); Balick *et al.* (1992); and Bryce *et al.* (1994). The nebula is surrounded by two halos, shown in a deep [O I] $\lambda$ 6300 [Fig. 2(c)] image. The brighter inner halo is more structured than the larger outer halo. Strong edge brightening in the inner halo is clear. A cut across the one of the southeast edges shows that the edge is about 3'' wide and is three times brighter than the inner halo. There is extreme contrast because the inner halo is almost as faint as the outer halo in this emission line, unlike in [N II] and [O III]. However, faint radial spokes of [O I] emission are seen from the outer edge of the shell, extending into the inner halo. Edge brightening of the outer halo can also be seen in the [O I] $\lambda$ 6300 image. It is extremely circular with a radius of 109''. The edge brightening is well resolved (7'' on the southeast arc) and rather clumpy. Both the inner and outer halos emit diffuse [O III] $\lambda$ 5007, but edge brightening in this emission line is just barely seen in the inner halo only (emission is  $\sim$ 10% brighter in the edge). A deep  $H\alpha$ + [N II] $\lambda$ 6583 emission-line image formed by summing all the frames in the data cube also shows the loops, filaments, and arcs seen in the [O I] image. Emission from the two lines can be separated using band integration. Overall, [N II] is  $\sim$ 2.0 times stronger than  $H\alpha$  in the halo. Our observations confirm the finding of Moreno & López (1987) that most of the fine structure in the halo seen in the light of  $H\alpha$  and [N II] is due to [N II] emission. The [N II] edge brightening is  $\sim$ 7%–25% brighter than [N II] inner halo emission. In contrast, the  $H\alpha$  halo emission is relatively smooth. An azimuthal average of  $H\alpha$  emission in the outer halo, fit with a power law, shows emission decreasing in brightness as  $r^{-\alpha}$ , where  $\alpha=1.85\pm 0.10$ , consistent with confinement of the outer halo (Frank *et al.* 1990). Halo emission is not seen in the summed interferograms from the [S II] data cube, but this is an artifact of our relatively brighter detection limits in this band.

### 3.2 Diagnostic Emission-Line Ratio Maps

#### 3.2.1 Balmer decrement

The  $H\alpha/H\beta$  map is shown in Fig. 3. Recall that the  $H\beta$  image was smoothed to match seeing with the  $H\alpha$  flux map. Careful attention was paid to the registration process, with registration accurate to  $\pm 0.1$  along rows and  $\pm 0.25$  along columns. Further refinement of the registration was accomplished by keying on the sharp increase in [N II] $\lambda$ 6583/ $H\beta$  ratio at the edge of the nebula (see Sec. 3.2.4). Duplicating the structure of the [N II] $\lambda$ 6583/ $H\alpha$  ratio provides registration accurate to  $\sim \pm 0.1''$ . As the variation in  $H\alpha/H\beta$  is less than 20%, this method produces good results. The flux calibration between the two frames (which would only affect the mean ratio) depends strongly on our ability to connect the separate red and green long-slit spectra accurately, and has an error bar of  $\sim \pm 6\%$  in the ratio.

The mean  $H\alpha/H\beta$  ratio in the map is  $3.74\pm 0.22$ . There is a smooth steepening of the Balmer decrement, to a ratio of  $\sim 3.93$ , around the 3/4 of the shell of the nebula. This steep-

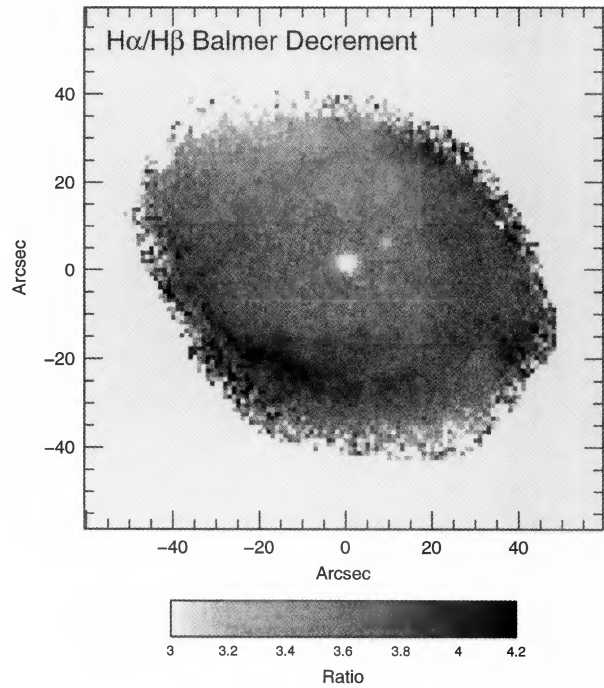


FIG. 3. Balmer decrement:  $H\alpha/H\beta$ .

ening is a smooth increase in Balmer decrement from the inner edge of the shell to the outer edge. Hawley & Miller (1977) noted a steepening to a ratio of 4.7 in one position of their aperture spectra of the Ring Nebula and attributed it to increased reddening as it appeared on only one of their apertures. The mean ratio in the inner 15'' of the nebula is 3.67, significantly lower than in the shell of the nebula (excepting the northeast side). The northeast side has a mean ratio of 3.39, and this does not have the same radial dependence as the ratio in the rest of the shell.

The Balmer decrement is slightly sensitive to temperature and we see a difference in the Balmer decrement between core and shell which is consistent with the expectation that the core is at a higher temperature than the shell. We observe a ratio of  $H\alpha/H\beta=3.68$  in the core compared to 3.74 (average) in the shell. If we correct for interstellar extinction by using our mean observed  $H\alpha/H\beta$  ratio of 3.74 and assuming the intrinsic ratio is 2.86 (the value for  $T_e=10\,000$  K,  $N_e=10^2$  cm $^{-3}$ , assuming Case B recombination as computed by Hummer & Storey 1987), then the corrected ratio in the center of the nebula is 2.81. This ratio is expected of a gas at  $T_e=13\,500$  K. Barker (1987) estimates an electron temperature of  $T_e=13\,000$  K in the  $O^{3+}$  region. Since it is expected that optical depth in the nebula varies as a function of position and that the gas is not perfectly Case B at all points, the lower Balmer decrement in the core could alternatively be due to stronger deviations from the assumption of Case B recombination. An examination of the  $H\gamma/H\beta$  ratio in our calibration long-slit spectra shows similar behavior as  $H\beta/H\alpha$ .

#### 3.2.2 [S II] density

The electron density ( $N_e$ ) was estimated using the [S II] $\lambda$ 6716/6731 line ratio using computed line strengths

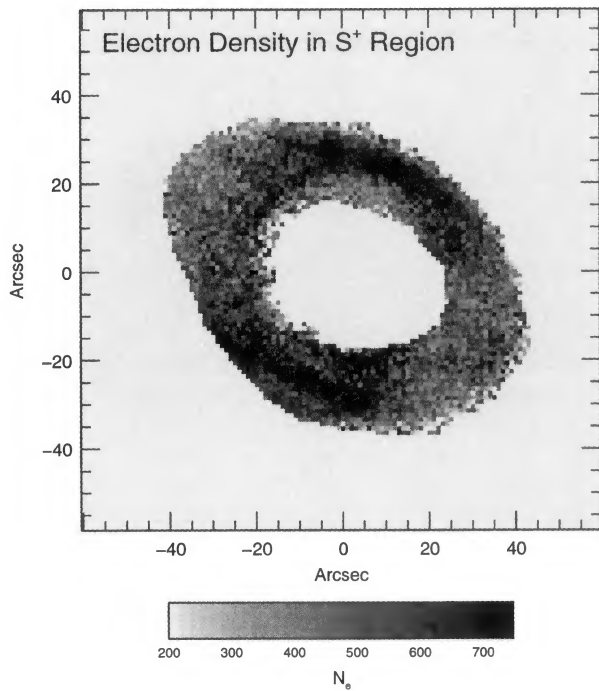


FIG. 4. Electron density in the  $S^+$  region. Density was calculated using the  $[S\text{ II}]\lambda 6716/6731$  line ratio for an assumed constant temperature of  $10^4$  K.

from Cai & Pradhan (1993), for an assumed constant electron temperature of  $10^4$  K. A map of  $N_e$  across the nebula is shown in Fig. 4. Since the density is derived from the line ratio of two lines originating in the same data cube, errors in the line ratio are relatively small. The major sources of error are uncertainty in fitting the continuum and in the line deblending procedure. The rms errors in the flux were  $\sim \pm 2\% - 3\%$  for most spectra. The precision of the derived  $N_e$  depends on the relation of  $N_e$  to the  $[S\text{ II}]$  ratio. For the range of  $N_e$  in this nebula, a  $\pm 3\%$  error in the  $[S\text{ II}]$  doublet ratio corresponds to  $\pm 70\text{ cm}^{-3}$  in  $N_e$ . The small systematic white-light correction applied to the  $[S\text{ II}]$  data cube only affects the average density, not the point-to-point density variations seen.

The highest density regions ( $N_e \sim 700\text{ cm}^{-3}$ ) appear as clumps in a broad band about the minor axis in the shell of the Ring. These density enhancements are located  $\sim 8''$  inward from the outer edge of the nebula (as defined as the sharp dropoff of  $H\alpha$  emission). The density is lower ( $N_e \sim 500\text{ cm}^{-3}$ ) in the rest of the nebula. It appears that the density enhancements extend in filaments toward and across the major axis on the inner edge of the shell. However, the  $[S\text{ II}]$  flux drops off rapidly at the inner edge of the shell, and so the density measurement is less certain. Band integration in the central region of the nebula does not show high density structure along the inner edge. Our density map is not entirely dissimilar to Kupferman's (1983) density map, but the higher spatial resolution of our map shows that the density enhancements in our map are resolved and appear quite sharp.

The density enhancements coincide with the general locations of some of the filaments identified in the  $[O\text{ I}]\lambda 6300$  emission image, but there is no detailed correlation. Projec-

tion effects would make it possible to see interior, sharp density enhancements if more filaments were crossed along the line of sight on the minor axis than on the major axis. In this case, the  $[S\text{ II}]$  density map and the  $[S\text{ II}]$  emission maps should look similar, but they do not (also noted by Kupferman 1983). An attempt to separate the filaments and the surrounding nebula into separate components showed that the filaments are not significantly more or less dense than in the general density map. Comparing the direct flux maps at  $[O\text{ I}]\lambda 6300$  and  $[S\text{ II}]$  that best show the filaments, we find no density contrast between the high surface-brightness filaments and the nebula in which they are embedded. We discuss this surprising result in Sec. 4.2 below.

### 3.2.3 $[N\text{ II}]$ temperature

The electron temperature ( $T_e$ ) was calculated using the  $[N\text{ II}]\lambda 6548+6583/5755$  line ratio following the five-level atom calculation of Osterbrock (1989), assuming a constant density of  $500\text{ cm}^{-3}$  (consistent with our mean  $N_e$  estimated from the  $[S\text{ II}]$  ratio map). The ratio was corrected for extinction as described in Sec. 2.4. Although the density map clearly shows that the density is not constant across the nebula, this simplifying assumption is acceptable as the electron temperature calculation is not very sensitive to electron density at our measured  $T_e$  and  $N_e$ .

Uncertainties in the  $[N\text{ II}]$  ratio map are dominated by the signal to noise in the direct image of the weak  $[N\text{ II}]\lambda 5755$  line. An estimate of the uncertainty in the  $[N\text{ II}]\lambda 5755$  image was made in the following way. Although the seeing was  $1.5''$ , the initial pixel size before binning was  $0.5''$ . The standard deviation of a running mean of a  $3 \times 3$  box (within the seeing disk) was taken to be an estimate of  $\sigma$ . This is an overestimate in areas where the emission is changing rapidly, such as at the edge of the shell. In the brightest regions, errors in flux are approximately  $\pm 10\%$ . Because the ratio map was derived from images not taken at the same time and in the same manner ( $[N\text{ II}]\lambda 6548, 6583$  are from a data cube,  $[N\text{ II}]\lambda 5755$  is from a direct image), a determination of the errors must also include the additional data reduction steps of registration and flux calibration. Emission from the nebula drops off sharply, and so errors in registration are very obvious in line-ratio maps. We are confident of our image registration, with errors estimated to be  $\pm 0.15''$ . Errors in the flux calibration factor (which would effectively shift the mean temperature up or down) we estimate to be about  $\pm 3\%$ , dominated by the uncertainty in the calibration of the  $[N\text{ II}]\lambda 5755$  image (due to the weakness of the line in our long-slit spectra). A  $\pm 10\%$  error in the  $[N\text{ II}]$  ratio corresponds to  $\sim \pm 375\text{ K}$  at a temperature of  $9900\text{ K}$ , but this is an absolute error, and we are much more sensitive to relative temperature variations.

The resulting  $[N\text{ II}]$  temperature map (Fig. 5) shows a smooth, fairly constant temperature distribution across the nebula. The mean temperature is  $9643\text{ K}$  with a standard deviation of  $230\text{ K}$  (disregarding the noisy center and edge pixels). Barker's (1987) aperture spectra give a mean  $[O\text{ III}]$  temperature of  $10\,000\text{ K}$  and a mean  $[N\text{ II}]$  temperature of  $9400\text{ K}$ . However, our mean  $[N\text{ II}]\lambda 6583/5755$  ratio (not corrected for extinction) is 75, which is comparable to Barker's

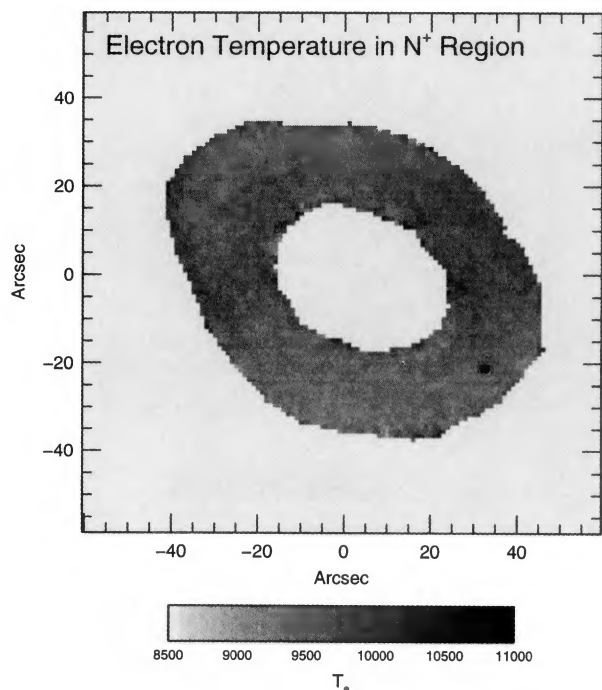


FIG. 5. Electron temperature in the  $N^+$  region. Temperature was calculated using the  $[N\text{ II}]\lambda 6548+6583/5755$  line ratio following Osterbrock (1989), assuming a constant electron density of  $500\text{ cm}^{-3}$ .

(1987) median ratio of 85. The difference in temperature is partly due to using different atomic constants (Barker uses Osterbrock 1974). Kupferman's (1983) mean  $[O\text{ III}]$  electron temperature is 150 K lower than our average  $[N\text{ II}]$  electron temperature. Our calibration long-slit spectra include the  $[O\text{ III}]\lambda 4363$  emission line, and confirm that the  $[O\text{ III}]$  temperature is higher than the  $[N\text{ II}]$  temperature in the Ring Nebula. Thus, Kupferman's (1983)  $[O\text{ III}]$  electron temperature is probably too low. Kaler (1986) predicts a nebula with  $\text{He II } \lambda 4686 = 0.24H\beta$  should have an  $[O\text{ III}]$  temperature of 11 092 K and a  $[N\text{ II}]$  temperature of 10 300 K.

Azimuthal averaging of the temperature map shows a relatively flat curve in the main body of the nebula and there does not appear to be a systematic temperature trend with radius. The radial decrease in  $[O\text{ III}]$  electron temperature seen by Kupferman (1983) is not present in the  $[N\text{ II}]$  temperature (this behavior in both line ratios is also confirmed by our calibration long-slit spectra). This difference between the two temperature diagnostics in radial behavior is understandable since the  $N^+$  zone is expected to be confined to a smaller radial extent than the  $O^{++}$  zone. Could we be missing temperature variations due to the poorer seeing in the  $[N\text{ II}]$  images? Possibly, but we note that filamentary structure is still apparent in a  $[O\text{ I}]$  flux image smoothed to  $3''$ , so it is unlikely that strong temperature differences between the filaments and the surrounding gas are being missed by our temperature map. More significantly, our long-slit spectra, taken in  $1.5''$  seeing, confirm a lack of temperature contrast between the filaments and their surroundings.

### 3.2.4 Ionization structure

Maps of the diagnostic emission-line ratios:  $\text{He II } \lambda 4686/H\beta$ ,  $[O\text{ I}]\lambda 6300/[O\text{ III}]\lambda 5007$ ,  $[O\text{ III}]\lambda 5007/H\beta$ ,  $[O\text{ I}]\lambda 6300/$

$H\beta$ ,  $[N\text{ II}]\lambda 6583/H\alpha$ , and  $[S\text{ II}]\lambda 6717+6731/H\beta$  are shown in Fig. 6. Line ratios formed from the Fabry-Perot spectral maps have been masked, showing zeros where no fits can be made because of low S/N. Ratios formed entirely from direct imaging show mostly noise outside the visible shell of the nebula.

The most striking feature of these line ratio maps is the very sharp drop in ionization coincident with the sharp drop in emission at the edge of the nebula. This sharp ionization edge is resolved, with a width of  $\sim 4''$  in the  $[O\text{ I}]/[O\text{ III}]$  map. The ionization edge also appears clumpy, particularly in this image. This ionization edge is elliptical in form, following the outer edge of the shell, but it is irregular at the extreme major axis ends and more clumpy and broken out than along the minor axis sides of the nebula (in the sense of extending to larger projected radius than expected for a simple ellipse).

The center of the nebula also has ionization structure as shown in both the  $\text{He II } \lambda 4686/H\beta$  and the  $[O\text{ III}]\lambda 5007/H\beta$  map. The inner ionization edge (between  $[O\text{ III}]\lambda 5007/H\beta$ ) is nearly circular in shape like the He II emission, not elliptical. It is also not continuous, but appears as several overlapping arcs.

### 3.3 Integrated Fluxes

The flux in each line was measured in a  $100''$  diameter circular aperture centered on the central star (this included part of the halo). These fluxes, with respect to  $H\beta$ , are given in Table 3. For the data cubes, a correction was made for flux in the masked regions by using band integration fluxes. These corrections were less than 2%.  $H\beta$  and  $[O\text{ III}]\lambda 5007$  images were not corrected for nebular continuum, and line ratios have been adjusted using a 2.5% continuum contribution to  $H\beta$ , determined from Sept. 1992 images.

Most of the low ionization potential (LIP) line emission in the Ring Nebula is rather strong relative to  $H\alpha$ , even for a PN (Hawley & Miller 1977). A look at the PN samples of Campbell (1968), Kaler (1980), and Kondratjeva (1993) shows that only about  $\sim 10\%$  of PNs have stronger  $[O\text{ I}]$  and  $[N\text{ II}]$  emission (with respect to  $H\beta$ ).

Estimations of physical quantities based on the above integrated line strengths are given in Table 4. The mean Balmer decrement is 3.72. The line ratios for the entire nebula give  $[N\text{ II}]$  temperature  $T_e = 9540\text{ K}$  and  $[S\text{ II}]$  density  $N_e = 550\text{ cm}^{-3}$ .

## 4. DISCUSSION

The Balmer decrement,  $[S\text{ II}]$  density,  $[N\text{ II}]$  temperature, and ionization state maps show physical conditions inside the nebula. Although it would be best to know these parameters at each point in the nebula, we are limited to the integration along the line of sight, yielding two-dimensional images. These two-dimensional maps reveal patterns not seen in one-dimensional spectra: a sharp drop in ionization at the outer edge of the nebula, an increase in the Balmer decrement in part of the nebula, and significant density variations along the minor axis. The maps are used to study the ionization edge, the filaments, and the possible geometry of the nebula.

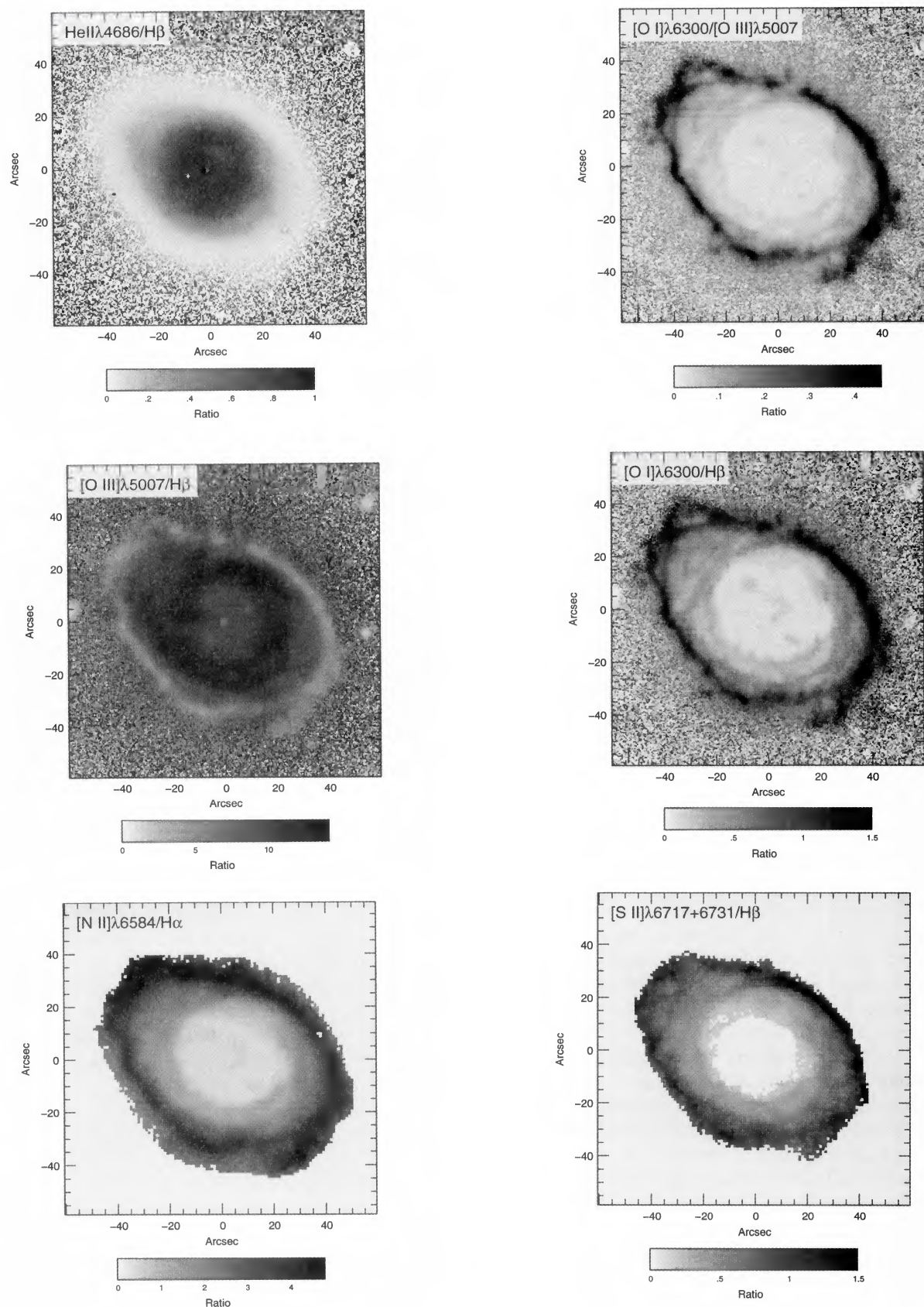


FIG. 6. Ionization structure ratio maps. The diagnostic emission-line ratios  $\text{He II } \lambda 4686 / \text{H}\beta$ ,  $[\text{O I}] \lambda 6300 / [\text{O III}] \lambda 5007$ ,  $[\text{O III}] \lambda 5007 / \text{H}\beta$ ,  $[\text{O I}] \lambda 6300 / \text{H}\beta$ ,  $[\text{N II}] \lambda 6584 / \text{H}\alpha$ , and  $[\text{S II}] \lambda 6717 + 6731 / \text{H}\beta$  are shown. Images are  $120''$  across. Line ratios formed from the data cube fits have been masked, showing zeros where no fits were made. Ratios formed entirely from direct imaging show mostly noise outside the visible shell of the nebula. Note that the mask for the  $[\text{S II}]$  data cube is smaller than the mask for the  $\text{H}\alpha$  data cube. The ionization edge is at the same position in both the  $[\text{N II}] / \text{H}\alpha$  and  $[\text{S II}] / \text{H}\beta$  ratio maps.

TABLE 3. Integrated line strengths.

Identification	$\lambda$	$F(\lambda)$	$I(\lambda)^a$
H $\beta^b$	4861	1.00	1.00
He II	4686	0.24	0.24
[O III]	5007	10.61	10.27
[N II]	5755	0.09	0.07
[O I]	6300	0.36	0.29
H $\alpha$	6563	3.72	2.86
[N II]	6583	6.41	4.92
[S II]	6717+6731	0.64	0.48

Observations integrated over 100" diameter circular aperture.

<sup>a</sup>Corrected for extinction using  $c=0.322$ .

<sup>b</sup> $F(\text{H}\beta)=2.45 \times 10^{-10} \text{ erg s}^{-1} \text{ cm}^{-2}$ .

#### 4.1 Ionization Edge

The ionization structure maps show a sharp drop in ionization state covering the entire outer edge of the shell. An ionization front in the Ring Nebula is expected since molecular hydrogen is detected in the halo (Zuckerman & Gatley 1988; Kastner *et al.* 1994). In the [O I]/[O III] ratio map, this ionization edge appears very clumpy in that there are multiple breaks in the high [O I]/H $\beta$  and [O I]/[O III] rims around the edge of the nebula. The density map does not show actual dense clumps of material; only ionization variations are seen. The clumpiness at the ionization front may explain the partially ionized halos observed around the Ring Nebula. Mechanisms for ionization of the inner and outer halos have been discussed in several papers (Zuckerman & Gatley 1988; Balick *et al.* 1992; Bryce *et al.* 1994; Kastner *et al.* 1994). The outer, spherical halo is unlikely to be the projection of a bipolar halo because it is too perfectly round (that would imply an inclination angle of exactly 0°). Instead, the outer halo may be partially ionized from radiation leaking through the ionization front. The radial spokes of [O I] seen outside shell could be shadowed regions behind dense clumps, with radiation leaking between the spokes. Such a situation is seen in the Helix Nebula on its inner edge (Meaburn *et al.* 1992).

The radial increase in Balmer decrement towards the outer edge of the shell is most likely due to differential reddening in the nebula. Regions of large H $\alpha$ /H $\beta$  in the shell of the nebula are spatially correlated with regions of strong molecular hydrogen emission observed by Zuckerman & Gatley (1988). Their H $_2$   $v=1 \rightarrow 0$  S(1) flux map shows emission from molecular hydrogen at the outer edge of the shell. The H $_2$  emission is weakest on the northeast side where our map shows the lowest reddening, and strongest near the region of largest Balmer decrement. A recent H $_2$  flux map by Kastner

*et al.* (1994) shows H $_2$  emission is spatially correlated with [O I] emission, again increasing toward the outer edge of the shell. The variations in Balmer decrement in the shell are thus consistent with reddening due to dust, probably in a neutral atomic and molecular sheath surrounding the ionized gas shell.

#### 4.2 Filaments

We find that the filaments are not significantly denser or cooler than the surrounding nebula. Our results disagree with the measured densities of Boeshaar (1974) in the Ring Nebula filaments of 4000–11 000 cm $^{-3}$  using the [S II] doublet, but confirm Kupferman's (1983) low-resolution electron density map which did not show higher densities in the filaments. Although the density enhancements coincide with some of the filaments, a density structure that follows the filament structure (most obviously traced in the [O I] flux map) is not seen. The temperature map is smooth and shows no filamentary structure even though the filaments are prominent in the [N II] flux maps. Our data show no density or temperature differences between the filaments and surrounding gas, only variations in ionization state (i.e., enhanced [O I], [N II], and [S II] emission in spatially sharp regions).

The lack of temperature and density differences between the filaments and the rest of the nebula is unexpected since only models composed of cool, dense filaments have been able to explain the high levels of [O I] and [N II] in certain PNs. A successful model for the Helix Nebula (Capriotti 1973) was composed of an optically thin gas with filaments (which were the shadowed regions behind optically thick condensations) that were 1.7 times denser than the adjacent nonshadowed regions and had a temperature of 6000 K. The densities and temperatures we measure for the filaments in the Ring Nebula do not show similar conditions as in this model. The Helix Nebula is similar to the Ring Nebula in its morphology, filamentary appearance, and strong [N II] and [O I] emission. However, its filaments are predicted and observed to be radial, unlike the filaments in the Ring Nebula, which also indicates that the Ring Nebula filaments are not the same structures as observed (and explained) in the Helix Nebula.

There must be a reason that the filaments in the Ring Nebula are in a different ionization state than the rest of the nebula. There are two possibilities. One is that there really are differences in temperature and density in the filaments that we have not detected, either because the variations are low contrast or are strongest on small spatial scales and very high spatial resolution would be needed to see them. The other is that the filaments simply represent local variations in ionization at the nebula edge and not dense condensations embedded within. The clumpy nature of the edge (seen in the [O I]/[O III] map, Fig. 6) might be reflecting an overall filamentary edge to the nebula. Possibly the ionization "edge" is not a smooth surface but a network of filaments.

#### 4.3 Nebular Geometry

Many different models have been proposed for the geometry of the Ring Nebula. The most recent model, based on the interacting stellar winds theory of PN evolution, is by

TABLE 4. Integrated spectroscopic properties.

H $\alpha$ /H $\beta$	3.72
$c$	0.322
$A_V$	0.688
[N II] $\lambda$ 6583+6548/5755	93.7
$T_e$	9540 K
[S II] $\lambda$ 6717/6731	1.011
$N_e$	550 cm $^{-3}$

Bryce *et al.* (1994). From observations of kinematics in the halo, they surmise that the nebula consists of a dense equatorial band (what we call the shell) with a bipolar inner halo. The outer halo is the relatively undisturbed red giant envelope (RGE) wind. An unresolved question with their model is the larger than expected observed ellipticity of the shell, as compared to the ellipticity of the inner halo and their estimate of the nebula's inclination angle. We propose that the shell of the Ring Nebula is an intrinsically oval torus, a geometry which can be explained by the observed density structure.

The shell of the Ring Nebula is thought to be a toroid because strong emission lines from the shell are nonspherical (Kupferman 1983). Besides showing a lack of low ionization emission in the center of the nebula, our observations further support a toroid geometry. The thickness of the nebula along the line of sight at each point in the nebula can be estimated using our electron density map and our  $H\beta$  flux map, since  $F(H\beta)$  goes as  $\int N_e N_p dV$ . The average thickness, given filling factor  $\epsilon$ , is about  $2 \times 10^{17} \epsilon^{-1}$  cm (assuming a distance of 600 pc). The brightest emission areas (along the minor axis) are not substantially thicker than the rest of the nebula (assuming a uniform and constant filling factor throughout the shell). The increased emission from the minor axis is therefore due entirely to the higher density observed along the minor axis. Our observations are consistent with a toroidal geometry for the shell.

Projection effects from tilting the toroidal shell cannot account for the large ellipticity of the outer edge of the shell (axis ratio of 0.7 indicating a tilt of  $45^\circ$ ). Suggestions that the Ring Nebula is bipolar and viewed at a small angle to the polar axis (Minkowski & Osterbrock 1960; Volk & Leahy 1993) have been confirmed by kinematic observations of the halo (Bryce *et al.* 1994). We also estimate the tilt of the shell by looking at the [O I] morphology. The filamentary [O I] $\lambda 6300$  emission-line flux image [Fig. 2(b)] is suggestive of a tilted cylinder geometry (see, for example, the model images in Frank *et al.* 1993), where the filaments trace out the ends of a cylindrical inner wall to the shell. Assuming this geometry, from the positions of the [O I] filaments we estimate that the tilt of the nebula is  $\sim 30^\circ$ , and the height of the cylindrical inner wall is  $13''$  ( $1.2 \times 10^{17}$  cm at a distance of 600 pc). This height is in reasonable agreement with the thickness estimated above, but the tilt angle is much lower than would be estimated from the ellipticity of the outer edge of the shell ( $45^\circ$ ) (the tilt is consistent, however, with the ellipticity of the inner halo; Bryce *et al.* 1994). Since the outer edge of the shell is more elliptical than can be accounted for by tilt projection, the shell of the nebula must be intrinsically oval in shape.

We look to the observed density structure to explain the oval shape of the shell. The current theory of PN evolution accepts density structure as the cause of asymmetrical evolution, specifically, evolution of a PN into a bipolar nebula is caused by a density gradient from equator to pole. The shaping of the nebula occurs as a fast tenuous wind from the central star interacts with a previous slow dense wind. When there is a density contrast in the slow wind, the fast wind encounters lower density along the polar axis and will accel-

erate faster in that direction, producing a bipolar nebula. Analogously, the density contrast observed in the Ring Nebula between the major and minor axes may be responsible for the fragmentation of the nebular shell along the major axis first.

The gas in an evolved nebula like the Ring Nebula has already undergone so much hydrodynamic shaping that it will be difficult (or impossible) to determine the origin of the high density structure from our observations. Either the high density region as we see it now was inherent in the mass-loss wind, or is the result of a snowplow effect. The morphology of the observed density enhancements does not match either case. The observed density enhancements are clumpy and not a smooth gradient as is usually assumed in theoretical models. Also, hydrodynamic models show the initial smooth density gradient to be snowplowed by shocks into density enhancements at the inner and outer edge of the shell (Frank 1994), not in the interior as seen in our density map.

## 5. CONCLUSIONS

This combination of observing techniques has produced line-emission and line-ratio maps of high accuracy and good spatial coverage. These properties are essential for investigating the physical conditions in large-scale structures in the nebula.

We see no density or temperature differences between the filaments and surrounding nebular gas. This leaves no explanation for the strong [O I] and [N II] emission in the filaments. Further observations which can put strong limits on the temperature and density difference between the filaments and surrounding nebula are needed. Recently, it has been shown that the properties of some fine structure features in other PNs are not entirely compatible with either photoionization or shock explanations (i.e., FLIERS, Balick *et al.* 1993). Thus, it is important to determine if the properties of the filaments in the Ring Nebula can be explained by the established theories of their origin and structure or if they have something in common with unexplained fine structure features in other PNs.

Our data are consistent with a intrinsically elliptical toroid geometry for the shell, which can be explained by the observed density structure using the principles of the interacting stellar winds theory. The density structure in the shell and its part in the evolution of the nebula should be more rigorously considered, since the density structure is a critical parameter in hydrodynamic modeling. Current models (see Frank 1994; Mellema 1993) assume axisymmetry, which is starting to break down in the Ring Nebula. The Ring Nebula might make a good example case for triaxial models since its structure is fairly uncomplicated (unlike highly structured PN such as NGC 6543).

We would especially like to thank Ray Bertram for help observing and Mark Wagner at Lowell Observatory. We are grateful to Bruce Balick and Julie Lutz for arranging the loan of a He II filter from Manastash Ridge Observatory. We

would like to thank Alice Quillen and Brad Peterson for their comments on the paper. We also appreciate useful discussions with Bruce Balick, and preprints sent by Adam Frank. IFPS instrument development was supported by NSF Grants

AST-8822009 and AST-9112879 and research was supported by an OSU Office of Research Seed Grant. The SIMBAD database of the Strasbourg, France ADC was used for some of the bibliographic research.

## REFERENCES

- Atherton, P. D., Hicks, T. R., Reay, N. K., Worswick, S. P., & Smith, W. H. 1978, *A&A*, 66, 297
- Balick, B. 1987, *AJ*, 94, 671
- Balick, B. 1993, Proceedings of IAU Symposium No. 155, edited by R. Weinberger and A. Acker (Kluwer, Dordrecht), p. 131
- Balick, B., Gonzalez, G., Frank, A., & Jacoby, G. 1992, *ApJ*, 392, 582
- Balick, B., Rugers, M., Terzian, Y., & Chengalur, J. 1993, *ApJ*, 411, 778
- Barker, T. 1987, *ApJ*, 322, 922
- Boeshaar, G. 1974, *ApJ*, 187, 283
- Brocklehurst, M. 1971, *MNRAS*, 153, 471
- Bryce, M., Balick, B., & Meaburn, J. 1994, *MNRAS*, 266, 721
- Cai, W., & Pradhan, A. K. 1993, *ApJS*, 88, 329
- Campbell, W. A. 1968 *PASP*, 80, 689
- Capriotti, E. R. 1973, *ApJ*, 179, 495
- Capriotti, E. R., Cromwell, R. H., & Williams, R. E. 1971, *ApJ*, 7, L241
- Cardelli, J. A., Clayton, G. C., & Mathis, J. S. 1989 *ApJ*, 345, 245
- Chu, Y.-H., Jacoby, G., & Arendt, R. 1987, *ApJS*, 64, 529
- Curtis, H. 1918, *Publ. Lick Obs.* 13, 57
- Dufour, R. J., & Quigley, R. 1993, Proceedings of IAU Symposium No. 155, edited by R. Weinberger and A. Acker (Kluwer, Dordrecht), p. 198
- Frank, A. 1994, *AJ*, 107, 261
- Frank, A., Balick, B., Icke, V., & Mellema, G. 1993 *ApJ*, 404, L25
- Frank, A., Balick, B., & Riley, J. 1990 *AJ*, 100, 1903
- Greenhouse, M. A., Hayward, T. L., & Thronson, H. A. 1988, *ApJ*, 325, 604
- Hawley, S. A., & Miller, J. S. 1977, *ApJ*, 212, 94
- Hummer, D. G., & Storey, P. J. 1987, *MNRAS*, 224, 801
- Jacoby, G. H., Quigley, R. J., & Africano, J. L. 1987, *PASP*, 99, 672
- Kaler, J. B. 1980, *ApJ*, 239, 592
- Kaler, J. B. 1986, *ApJ*, 308, 322
- Kastner, J. H., Gatley, I., Merrill, K. M., Probst, R., & Weintraub, D. A. 1994, *ApJ*, 421, 600
- Kondratjeva, L. N. 1993, Proceedings of IAU Symposium No. 155, edited by R. Weinberger and A. Acker (Kluwer, Dordrecht), p. 195
- Kupferman, P. N. 1983, *ApJ*, 266, 689
- Kwok, S., Purton, C. R., & Fitzgerald, P. M. 1978, *ApJ*, 219, L125
- Meaburn, J., Walsh, J. R., Clegg, R. E. S., Walton, N. A., Taylor, D., & Berry, D. S. 1992, *MNRAS*, 255, 177
- Mellema, G. 1993, Ph.D. thesis, Leiden University
- Minkowski, R., & Osterbrock, D. E. 1960, *ApJ*, 131, 537
- Moreno, M. A., & Lòpez, J. A. 1987, *A&A*, 178, 319
- Osterbrock, D. E. 1974, *Astrophysics of Gaseous Nebulae* (Freeman, San Francisco)
- Osterbrock, D. E. 1989, *Astrophysics of Gaseous Nebulae and Active Galactic Nuclei* (University Science Books, Mill Valley)
- Pogge, R. W. 1991, OASIS; An Imaging Fabry-Perot Reduction Package, OSU Astronomy Internal Report 91-02
- Pogge, R. W. 1992, in *Astronomical CCD Observing and Reduction Techniques*, edited by S. Howell, ASP Conf. Ser., 23, 195
- Pogge, R. W., Owen, J. M., & Atwood, B. 1992, *ApJ*, 399, 147
- Reay, N. K., & Worswick, S. P. 1977, *MNRAS*, 179, 317
- Richer, M. G., McCall, M. L., & Martin, P. G. 1991, *ApJ*, 377, 210
- Volk, K., & Leahy, D. 1993, *AJ*, 106, 1954
- Weinberger, R. 1989, *A&AS*, 78, 301
- Williams, R. E. 1973, *MNRAS*, 164, 111
- Zuckerman, B., & Gatley, I. 1988 *ApJ*, 324, 501